

The Radius Distribution of M dwarf-hosted Planets and its Evolution

Eric Gaidos^{1,2}, * Aleezah Ali³, Adam L. Kraus⁴, Jason F. Rowe⁵

¹Department of Earth Sciences, University of Hawai'i at Mānoa, 1680 East-West Rd, Honolulu, HI 96822, USA

²Institute for Astrophysics, University of Vienna, Türkenschanzstrasse 17, 1180 Vienna, Austria

³Institute for Astronomy, University of Hawai'i at Mānoa, 2680 Woodlawn Drive, Honolulu, HI 96822, USA

⁴Department of Astronomy, University of Texas at Austin, 2515 Speedway Stop C1400, Austin, TX 78712, USA

⁵Department of Physics & Astronomy, Bishop's University, 2600 College Street Sherbrooke, QC, Canada, J1M 1Z7

ABSTRACT

M dwarf stars are not only the most promising hosts for detection and characterization of small and potentially habitable planets, they provide leverage relative to solar-type stars to test models of planet formation and evolution. Using *Gaia* astrometry, adaptive optics imaging, and calibrated gyrochronologic relations to estimate stellar properties, filter binaries, and assign ages, we refined the radii of 179 transiting planets orbiting 119 single late K- and early M-type stars detected by the *Kepler* mission, and assigned stellar rotation-based ages to 115 of these. We constructed the radius distribution $< 4R_{\oplus}$ planets and assessed its evolution with time. As for solar-type stars, the inferred distribution contains distinct populations of “super-Earths” (at $\sim 1.3R_{\oplus}$) and “sub-Neptunes” (at $\sim 2.2R_{\oplus}$) separated by a gap or “valley” at $\approx 1.7R_{\oplus}$ that has a period dependence that is significantly weaker (power law index of $-0.026^{+0.026}_{-0.017}$) than for solar-type stars. Sub-Neptunes are largely absent at short periods (< 2 days) and high irradiance, a feature analogous to the “Neptune desert” observed around solar-type stars. The relative number of sub-Neptunes to super-Earths declines between the younger and older halves of the sample (median age 3.8 Gyr), although the formal significance is low ($p = 0.06$) because of the small sample size. The decline in sub-Neptunes appears to be more pronounced at long orbital periods vs. short periods; this is not due to detection bias and could indicate that these objects are inflated by a mechanism that operates at elevated irradiance, e.g. a runaway water greenhouse augmented by H/He.

Key words: stars: pre-main sequence – planetary systems – planet-star interactions – planets & satellites: protoplanetary disks – open clusters and associations

1 INTRODUCTION

The launch of the *Kepler* mission in 2009 (Borucki et al. 2010) ushered in a revolution in the study of planetary systems, the occurrence of rocky, Earth-like planets, and the potential for habitable and life-hosting planets in the Galaxy. *Kepler* revealed a population of small (Earth- to Neptune-size) planets on close-in orbits around solar-type stars (e.g., Burke et al. 2015; Hsu et al. 2019; Bryson et al. 2021). Analyses showed that the occurrence of these planets increases with decreasing stellar mass or later spectral type (Dressing & Charbonneau 2015; Mulders et al. 2015; Gaidos et al. 2016; Hardegree-Ullman et al. 2019; Ment & Charbonneau 2023). This trend is important to the search for Earth-like planets since the low luminosities and compact “habitable zones” of M dwarfs mean that they have the potential to host many rocky planets with temperate climates; the elevated space density of M dwarfs relative to their solar-mass counterparts (Smart et al. 2021; Ravinet et al. 2022) means that many host stars are nearby and can thus be prime targets

for follow-up observations to detect and characterize atmospheres, e.g., by *JWST* (Greene et al. 2023; Zieba et al. 2023),

However, M dwarfs differ from their solar-mass counterparts in ways that could impact the properties and evolution of planets, including an extended pre-main sequence phase, longer rotational spin-down times, and elevated X-ray and extreme ultraviolet emission relative to bolometric emission. There may also be differences in their protoplanetary disks, i.e. their masses (Gaidos 2017), lifetimes (Silverberg et al. 2020), and chemistry (Tabone et al. 2023). To assess potential variation in planetary evolution, precise measurement of the properties of a large number of planets in systems with robust ages that span a wide age range is needed. Currently, the confirmed and candidate transiting planets among the *Kepler* Objects of Interest (KOIs) provide the largest, most uniform, and most precisely measured set of planet properties, i.e., radii and periods (e.g., Thompson et al. 2018).

The radius distribution of sub-Jovian planets around solar-type stars detected by the *Kepler* mission contains two distinct peaks, representing populations of “super-Earths”- and “sub-Neptunes” separated by a gap or “valley” at $\sim 1.7R_{\oplus}$ (Owen & Wu 2013; Fulton et al. 2017; Berger et al. 2020). Complementary measurements

* E-mail: gaidos@hawaii.edu.

of planet mass (and hence density) indicate that sub-Neptunes and super-Earth have rocky cores with and without envelopes of volatile, low molecular-weight constituents (Weiss & Marcy 2014; Rogers 2015). These envelopes could consist of hydrogen and helium captured from the primordial gas disk during planet formation (e.g., Béthune & Rafikov 2019), and/or H₂O and other volatiles acquired as ices (Turbet et al. 2020; Luque & Pallé 2022). Unfortunately, mass measurements of small planets are observationally expensive, often not always precise, and the different mass-radius relations are at least partly degenerate (e.g., Rogers & Seager 2010).

Pursuing an alternative approach, numerous statistical studies have made inferences about the nature of these planets and their manner of their evolution by correlating variation in the radius distribution with parameters such as orbital period (semi-major axis) and host star mass (Zhu & Dong 2021, and references therein). The former sets the stellar irradiation of the planet and the latter – with M dwarfs at one extreme – governs the timescale over which that irradiation changes (Barnes et al. 2009; Johnstone et al. 2021). Due to their faintness, limited inclusion in the *Kepler* survey, and more poorly understood properties of M dwarf stars, studies of their planets’ radius distribution have lagged those of solar-type stars (e.g., Dressing & Charbonneau 2015; Gaidos et al. 2016; Hirano et al. 2018; Kanodia et al. 2019).

The question of planetary evolution has also been addressed directly by looking for variation with host star age. Among FGK stars, the number of sub-Neptunes (with envelopes) relative to super-Earths (without envelopes) planets is found to decrease with age (Berger et al. 2020; Sandoval et al. 2021; David et al. 2021; Chen et al. 2022), consistent with cooling and contraction of the envelopes and/or escape of light elements to space (e.g., Howe & Burrows 2015). The mean size of sub-Neptunes may also decrease with time (Chen et al. 2022) – but see Petigura et al. (2022).

Reconstructing the planet radius distribution of M dwarf planets and its evolution requires radii and ages that are more precise and accurate than have previously been available. Transiting planet radius depends on host star radius, and calculations of the radius distribution that account for detection efficiency require stellar density (both mass and radius). New empirical calibrations for M dwarfs permit estimation of mass and radius based on the precise absolute luminosities made possible by *Gaia* parallaxes (Mann et al. 2015, 2019). Moreover, both *Gaia* astrometry and ground-based adaptive optics (AO) allow more thorough vetting for stellar companions, which can affect the radius estimate. Binary stars also appear to have a planet population distinct from single stars (Kraus et al. 2016; Sullivan et al. 2023).

For field M dwarfs, rotation (gyrochronology) is the most promising method to assign ages compared to other techniques (i.e., isochrone-fitting, asteroseismology, depletion of lithium, or kinematics), but in the absence of accurate, first-principles spin-down models, this approach requires empirical calibration. Dungee et al. (2022) constructed a rotation sequence (vs. effective temperature T_{eff}) for late K-type and early-type M dwarfs in the 4 Gyr-old M67 cluster, allowing calibrated age-dating of $T_{\text{eff}} \approx 3200\text{--}4200\text{K}$ stars to nearly half the age of the Galactic disk. Moreover, a comparison with younger clusters suggests these stars are spinning down according to a simple power-law prescription (Skumanich 1972) by ages of a few Gyr, justifying an extrapolation to older ages. Gaidos et al. (2023b) constructed T_{eff} -dependent age-rotation relations using rotation sequences and assigned ages to the cool host stars of known exoplanets, including *Kepler*-confirmed and candidate planets.

In this work we revise the radius distribution of *Kepler* planets around single late K- and early M-type dwarf stars and examine its

variation with age, taking advantage of (1) precise *Gaia* parallaxes for luminosity calculations and revised mass/radius/luminosity relations based on nearby stars; (2) identification and screening of binary systems using astrometry and AO imaging; and (3) assignment of robust rotation-based ages based on a new gyrochronology (Gaidos et al. 2023a). We compare the M dwarf planet radius distribution to that derived for solar-type stars and interpret it and its change with time to different scenarios for planet composition and evolution.

2 ANALYSIS

We matched the Kepler Input Catalog (KIC, Brown et al. 2011) with *Gaia* Data Release 3 (DR3) sources (Gaia Collaboration et al. 2023) using an angular separation criterion of $<0''.71$. Absolute K_s -band ($2.2\ \mu\text{m}$) magnitudes (M_K) were computed using photometry from the 2MASS Point Source Catalog (Skrutskie et al. 2006; Cutri et al. 2013) and parallaxes from *Gaia* Data Release 3 (Gaia Collaboration et al. 2016, 2023). We restricted our analysis to stars observed by *Kepler* during Quarters 1-17 with $M_K > 4.5$ (inclusive of spectral types later than K5, Pécaut & Mamajek 2013), and that appear in the catalog of late K and M-type dwarfs for which Santos et al. (2019) obtained rotation signals from *Kepler* lightcurves (about 59% of the 24,162 stars they analyzed). We further limited the target sample to stars with T_{eff} values in Santos et al. (2019) between 3200 and 4200K, the limit of the gyrochronology which we apply to these stars (Gaidos et al. 2023b), yielding a final sample of 5433 target stars that *Kepler* observed with the relevant host star parameters. Around these stars we identified objects from the DR25 version of the *Kepler* Objects of Interest (KOI) catalog based on data from Quarters 1-17 (Thompson et al. 2018), excluding KOIs with Exoplanet Archive designations of “false positive”.¹ Finally, we restricted the sample to KOIs with gyrochronologic age assignments from Gaidos et al. (2023b).

Host star masses were calculated from an empirical mass-luminosity relationship in (Eqn. 4 in Mann et al. 2019). Radii were calculated from M_K using Eqns. 4 or 5 in Mann et al. (2015) for stars with or without estimates of [Fe/H] retrieved from the Exoplanet Archive.² Errors were estimated using Monte Carlo calculations assuming normally-distributed errors in K_s -band magnitudes and parallaxes.

2.1 Filtering of binary stars

Stars in binary or multiple systems with separations $\lesssim 50$ au are known to host a planet population that differs from that around single stars (Kraus et al. 2016). Furthermore, binary stars with separations (< 100 au) have different rotational histories than their single counterparts (e.g., Messina et al. 2017; Stauffer et al. 2018), meaning that a rotation-age relation developed for single stars cannot be applied. 90% of M dwarfs in the *Kepler* field are more distant than 135 pc, thus these physical separations correspond to angular separations $< 1''$. Other effects of companions or any nearby sources unresolved

¹ To maximize uniformity and the robustness of the statistics, we did not incorporate the DR25 Supplemental Catalog, which includes a few planets (candidates) erroneously categorized as false positives in DR25. https://exoplanetarchive.ipac.caltech.edu/docs/PurposeOfKOITable.html#q1-q17_sup_dr25

² These [Fe/H] estimates are typically from published analyses, to be distinguished from the metallicity estimates included in the original KIC.

or partially resolved by *Kepler* (which had 4" pixels and a 3.1-7.5" PSF) are that the transit signals are diluted and identification of the host star itself – and thus planet properties – may be ambiguous. The K_S -band photometry used to estimate radius and mass will be inaccurate for binaries that are unresolved by the 2MASS survey (resolution of $\sim 3''$). Thus we identified and excluded KOIs around binary stars with separations $< 4''$. Binary/multiple systems or candidate systems were identified and excluded using (1) *Gaia* astrometry of resolved sources; (2) *Gaia* astrometric error relative to single-star astrometric solutions; (3) adaptive optics imaging; and (4) over-luminosity relative to a single-star locus in a color-absolute magnitude diagram. Here the procedures and outcomes are summarized; details will be published in a forthcoming paper.

Gaia resolved companions: We identified companions resolved by *Gaia* (≥ 1 arcsec, Ziegler et al. 2018a) based on similarity of parallax (distance) and proper motion. Rather than fixed criteria for similarity (e.g., El-Badry et al. 2021), we adopted a Bayesian approach. We identified candidate companions with cone searches of the DR3 catalog with a radius of $74''$ (corresponding to about 10^4 au at the median distance of *Kepler* M dwarfs) around each *Kepler* M dwarf. We computed the probability of companionship as $P_{\text{binary}} = P_c / (P_c + P_b)$, where P_c and P_b are the likelihoods that the source is a companion or background star, respectively. We evaluated these assuming normally-distributed errors using:

$$P_c = \frac{\Delta\mu}{\sigma_{\Delta\pi} (\sigma_{\Delta\mu}^2 + \mu_{\text{orb}}^2)} \exp \left[-\frac{\Delta\mu^2}{2(\sigma_{\Delta\mu}^2 + \mu_{\text{orb}}^2)} - \frac{\Delta\pi^2}{2\sigma_{\Delta\pi}^2} \right], \quad (1)$$

and

$$P_b = \frac{1}{N-1} \sum_{i=1}^S \frac{\Delta\mu_i}{\sigma_{\Delta\pi} (\sigma_{\Delta\mu}^2 + \mu_{\text{orb}}^2)} \exp \left[-\frac{\Delta\mu_i^2}{2(\sigma_{\Delta\mu}^2 + \mu_{\text{orb}}^2)} - \frac{\Delta\pi_i^2}{2\sigma_{\Delta\pi}^2} \right]. \quad (2)$$

$\Delta\mu$ and $\sigma_{\Delta\mu}$ are the absolute scalar difference in proper motion between the star and source and its standard error, $\Delta\pi$ and $\sigma_{\Delta\pi}$ are the difference in parallax and its standard error, and μ_{orb} is a “softening” term that accounts for the angular orbital motion of a binary. This last term we set to 5 mas yr^{-1} based on Eqn. 4 in El-Badry & Rix (2018). Constant factors that divide out are omitted from Eqns. 1 and 2. The difference in the terms involving parallax and proper motion reflects the latter’s two-dimensionality. To improve the statistical accuracy by averaging over many stars, the summation for P_b is performed over the S stars in all the $N-1$ other cone searches (a few thousand stars) that cannot be companions. We imposed no weighting with angular separation other than the generous search radius. Based on the observed distribution of P_{binary} values relative to those calculated using stars from other fields, we identified a threshold of $P_{\text{binary}} > 0.98$ to select companions.

Gaia astrometric error: Binaries with separations $< 1''$ cannot be resolved by *Gaia* (Ziegler et al. 2018b) but can often be identified based on the poor fit of *Gaia* astrometry to a single-star solution (Belokurov et al. 2020). This is quantified as the Reduced Unit Weight Error (RUWE, Lindegren et al. 2018) and values significantly greater than unity are indicative of a multiple star system. We selected a threshold of 1.4 based on the distribution RUWE values of AO-identified binaries (Kraus et al., in prep.).

AO imaging: AO imaging of KOIs was obtained of 75 of 86 systems (116 of 139 planets) with the NIRC2 infrared imager and AO system on the Keck-2 telescope (McLean & Chaffee 2000). Observations used the narrow camera (10 mas pixel scale) and either

the K_{cont} or K_p filters. Images were processed, sources extracted, and astrometry performed using the pipeline described in Kraus et al. (2016). We selected those sources with separations $< 2''$ and contrast $\Delta K < 4$ as highly likely to be bound companions based on Kraus et al. (2016).

Photometry: Unresolved late K and M dwarf binaries can be identified by their over-luminosity relative to single stars on the main sequence since these stars evolve imperceptibly on the main sequence. Metallicity is the sole confounding factor, and differences in $[\text{Fe}/\text{H}]$ produce a dispersion in color-absolute magnitude relations.³ By experimenting with different color-magnitude combinations constructed from ground-based photometry, we found that a color-magnitude locus of *Kepler* M dwarfs constructed using PanSTARRS g -y vs. M_y (Tonry et al. 2012) has the smallest dispersion and is thus the least sensitive to metallicity. We identified stars that are more luminous than the best fit by more than two standard deviations as probable binaries.

2.2 Planet radius distribution

The posterior distribution in radius of each planet was determined by multiplying each value from the Monte Carlo Markov Chain (MCMC) posterior chains for planet-to-star radius ratio from DR25 Q1-17 (Hoffman & Rowe 2017) with a value from the stellar posterior distribution in radius calculated above, assuming Gaussian errors in magnitude and parallax. We normalized each distribution by the summed probability for detection of an equivalent planet around every star observed by *Kepler* that is a late K- or early M-type dwarf $M_K > 4.5$, $3200 < T_{\text{eff}} < 4200\text{K}$ and that appears in the Santos et al. (2019) catalog of stars evaluated for rotation periods. We used the KeplerPORTs code (Burke & Catanzarite 2017b) to calculate the probability of detection (including the geometric transit probability). The required window functions, one-sigma detection functions (Burke & Catanzarite 2017a), “dataspans” (timespans of data), and duty cycles were retrieved from the NASA Exoplanet Archive. Non-linear (four-coefficient) limb-darkening coefficients were obtained from the DR25 Stellar Properties Catalog (Mathur et al. 2017). To mimic the removal of binaries from the KOI list, we excluded all target stars with *Gaia* RUWE values > 1.4 . This distilled the catalog to 182 KOIs in 122 systems. Finally, KOIs were then matched with entries in the TIME Table of Gaidos et al. (2023b) to retrieve gyrochronologic age estimates. We identified 115 KOIs (76 systems) with entries in the tabulation of Gaidos et al. (2023a) with a median age of 3.86 Gyr. The summed probabilities over all stars represent the expected number of detections if each star in the observed sample had such a planet. Each posterior distribution in radius was divided by this quantity and then summed to give the number of objects per unit radius per star. As a metric of uncertainty due to radius error and finite counting statistics, we calculated 68% confidence intervals by constructing 1000 Monte Carlo realizations using bootstrap sampling of the planet population with replacement.⁴

³ Gravity does not vary significantly for a given T_{eff} among late K- and M dwarf stars and extinction is negligible at the distance of most M dwarfs observed by *Kepler*.

⁴ While multi-planet systems will affect the counting statistics of total planet occurrence (which is not considered here), correlation between the radii of planets in the same system (e.g., Weiss et al. 2018) would impact the significance of individual features.

2.3 Validation

To validate our methodology for reconstructing the planet radius distribution we constructed a sample of synthetic KOIs the same size as the actual one (115 planets, see Sec. 3), drawing radii from the sum of two Gaussian distributions representing super-Earths and sub-Neptunes. The fractional populations in the two distributions were set to 0.4 and 0.6, the centroids were set to 1.3 and 2.1 R_{\oplus} , and the standard deviations were set to 0.15 and 0.25 R_{\oplus} , respectively. Orbital periods were selected from a power-law distribution between 1 and 40 days that reproduces the observed distribution (Gaidos et al. 2016). The synthetic planets were randomly assigned to the *Kepler* late K/early M population with measured rotation periods as defined above. To calculate the planet-star radius ratio, the stellar radii were determined using the metallicity-dependent relation of Mann et al. (2015), with metallicities drawn from the Gaussian distribution found among *Kepler* M dwarfs Gaidos et al. (2016). However for added realism these artificial metallicities were not propagated to the analysis of synthetic KOIs since the metallicities of many KOIs are not well determined; instead, the metallicity-independent relation of Mann et al. (2015) was used. The *total* probability of detection (including the geometric factor) was calculated for each star-planet pair as described above and the pair accepted conditional to a random uniform draw below this probability. In lieu of actual posterior distributions for the *observed* radius ratio we adopted Gaussians with fractional standard deviation that are 1/SNR, where SNR is the predicted transit signal-to-noise (Howard et al. 2012):

$$\text{SNR} = \frac{\delta}{\sigma_{\text{CDPP}}} \sqrt{\frac{N\tau}{2 \text{ hr}}}, \quad (3)$$

where δ is the transit depth (approximately the radius ratio squared), σ_{CDPP} is the measured combined differential photometric precision of the star over 2 hours (Christiansen et al. 2012, 2 hr is a typical transit duration), N the number of transits (equal to the dataspan times the duty cycle divided by the orbital period), and τ the transit duration (after averaging over a uniformly distributed impact parameter). Host star-planet pairs were generated until the accepted number equaled the size of the actual sample

We ran the synthetic KOIs through the same analysis pipeline as the actual KOIs to produce a simulated observed radius distribution. This is plotted along with the input distribution in Fig. 1. The bimodal distribution is largely reproduced, but with a noticeable broadening of the super-Earth distribution, probably because of the absence of measured [Fe/H] "measurements" and the effect of noise on the radii of the smallest detectable planets. The input ratio of super-Earths to Neptunes (divided by the vertical grey line) is 0.74 while the retrieved ratio is 0.80, an increase of 8%. The increase is due to the greater scatter of the more poorly determined super-Earths into the sub-Neptune range compared to vice-versa. The location of the apparent valley is shifted to larger radii (from 1.64 to 1.74 R_{\oplus}) for the same reason.

3 RESULTS

We refined the radii of 179 KOIs around 119 single late K and early M dwarfs with matches to *Gaia* DR3 sources and rotation periods in Santos et al. (2019) (Table 4.2), of which 115 (72 systems) were assigned ages from Gaidos et al. (2023a). The two largest objects in the sample (excluded from further analysis) are the hot Jupiter KOI-254.01 (Kepler-45b, Johnson et al. 2012), and the 5.45 \pm 0.27 R_{\oplus} KOI-2715.01 (Kepler-1321b, Morton et al. 2016) orbiting a late K dwarf (neither shown in Fig. 2). The next largest planet is the 3.20 \pm

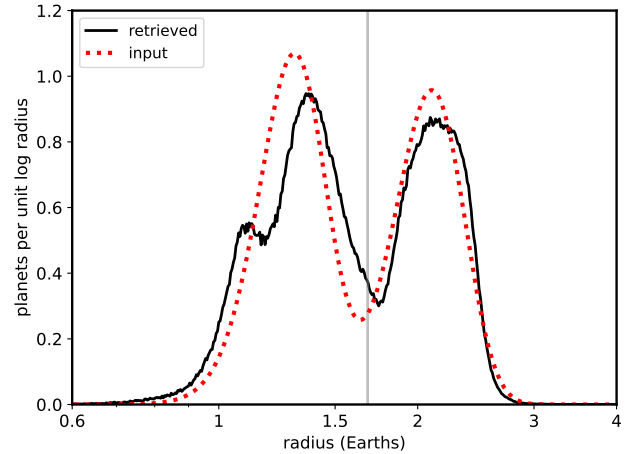


Figure 1. Radius distribution of simulated planets (red dotted curve) and distribution retrieved from 179 simulated KOIs (solid black curve). The vertical grey line at 1.68 R_{\oplus} is the approximate divide between super-Earths and sub-Neptunes found among actual KOIs.

0.14 R_{\oplus} sub-Neptune KOI-253.01 (Kepler-2000b, Valizadegan et al. 2023), highlighting how Neptune-size and larger planets are very rare around M dwarfs.

The detection efficiency-corrected radius distribution constructed from the other 113 KOIs (excluding the two largest objects discussed below) is shown by the black line in Fig. 2, with the grey region spanning the 68% confidence interval, and the radii and ages of the KOIs used in this reconstruction are listed in Table 4.2. The total occurrence is the integral over the distribution and is 1.87 planets per star. The planet radius distribution contains two prominent peaks at about 1.3 R_{\oplus} (super-Earths) and 2.2 R_{\oplus} (sub-Neptunes). There is a possible but not statistically significant third peak at 3 R_{\oplus} , consisting of four planets with a similar size. The super-Earths and sub-Neptunes peaks are separated by an intervening gap or "valley" around 1.6-1.7 R_{\oplus} , as first described for solar-type stars (Owen & Wu 2013; Fulton et al. 2017) and later tentatively identified around M dwarfs (Hirano et al. 2018; Van Eylen et al. 2021). The stellar mass range of our sample is 0.35-0.67 M_{\odot} , with a median of 0.59 M_{\odot} , and at the median orbital period of 7.1 days; with these, the mass- and period-dependent relation (Eqn. 11) of Ho & Van Eylen (2023) predicts a radius valley centered at 1.68 \pm 0.13 R_{\oplus} . This is in agreement with the distribution found in this sample (vertical red lines in Fig. 2).

The smallest planets in the sample are KOIs 5692.01 (0.55 \pm 0.04 R_{\oplus}) and 7793.01 (0.52 \pm 0.05 R_{\oplus}), around early M and late-K type dwarfs, respectively. The low detection probabilities of these small objects potentially inflate their occurrence and produce an apparent peak in the radius distribution, but this is not very statistically significant (grey zone in Fig. 2). KOI 314.03 (Kepler-138b), with a radius of 0.64 \pm 0.03 R_{\oplus} , makes a prominent contribution to the distribution at larger radii. The probability of detecting it in the overall sample is very low due to its respectable orbital period (10.3 days), thus it could represent a significant sub-population. However, this object is part of a system of at least three transiting planets, and it was only discovered after the system was analyzed with optimized, automated routines following the discovery of its larger cousins (Batalha et al. 2013).

We subdivided the planets with assigned ages into two nearly

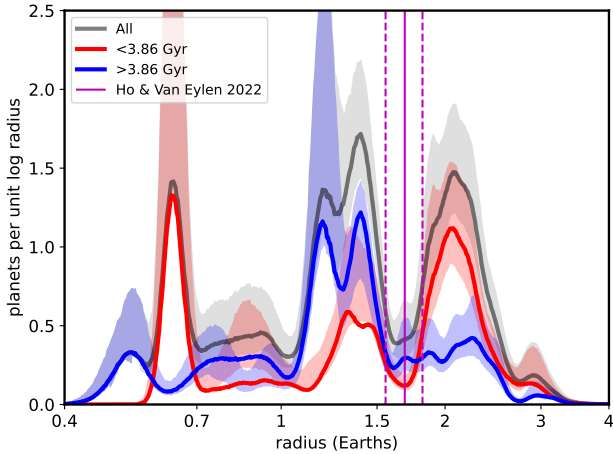


Figure 2. Empirical, non-parametric radius distribution of planets hosted by late K- and early M-type dwarfs observed by *Kepler* and assigned ages based on rotation, corrected for detection efficiency. The black line is the total distribution (113 planets), while the red and blue lines are the distributions for the halves of the sample with rotation-based ages younger and older than the median age of 3.86 Gyr, respectively. Shaded regions denote 68% confidence interval determined from Monte Carlo sampling with replacement. The vertical magenta lines mark the location (and uncertainty) of the radius valley using Eqn. 11 in Ho & Van Eylen (2023) for the sample’s median mass of $0.59 M_{\odot}$ and median period of 7.1 days.

equal halves based on the median gyrochronologic age (3.86 Gyr). The sub-Neptune peak is much less prominent in the older sample while the super-Earth is larger, with the ratio between the two (integrated over $1.68-4R_{\oplus}$ and $0.7-1.68R_{\oplus}$, respectively) declining from 2.67 to 0.59 from the younger to older moieties. This is consistent with the evolution of planets by the loss and/or contraction of low molecular-weight envelopes over time. Indeed, the integrated probabilities over mini-Neptunes ($1.7-4R_{\oplus}$) fall from 0.65 to 0.31 and is roughly equivalent to the increase in the Earth- and super-Earth ($0.7-1.7R_{\oplus}$) from 0.24 to 0.53. There is no evidence for a decrease in the mean radius of the sub-Neptunes with age nor a deepening of the radius valley as has been seen by other analyses of solar-type stars (Petigura et al. 2022; Chen et al. 2022) but the small sample size limits the robustness of this conclusion. Two-sided Kolmogorov-Smirnov and Anderson-Darling tests provide weak statistical support for the young and old samples to be drawn from different populations ($p = 0.056$ and 0.16 , respectively). A plot of radius vs. age (top panel of Fig. 3) shows that while sub-Neptunes decline relative to super-Earths with age, they are still numerous.

We investigated the sensitivity of this result to the choice of divisor age, since the choice of the median is a statistical convenience rather than being physically motivated. Moreover, the gyrochronologic ages have significant uncertainties which can “blur” age dependence. We thus investigated two other divisors; an age of 1.73 Gyr at which the difference between young and old radius distributions is maximized (minimum p -value from a two-sided Kolmogorov-Smirnov test) and an age of 2.8 Gyr which falls in a low density region of the age distribution (horizontal dashed and dotted lines in the top panel of Fig. 3). The two sets of alternative distributions are compared in the bottom panel of Fig. 3 and can be compared to that in Fig. 2. All three distributions exhibit an elevated ratio of sub-Neptunes to super-Earths in the younger population: in

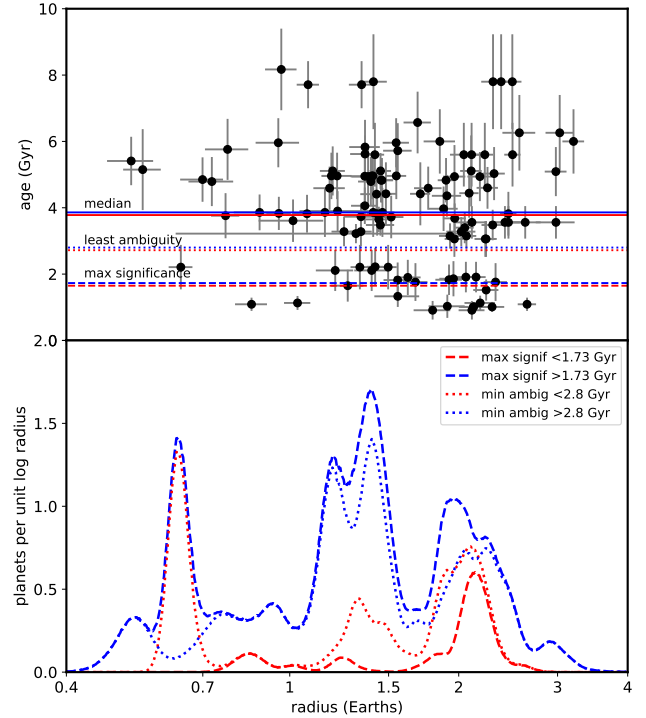


Figure 3. Top: Planet radius vs. gychronologic system age. Three possible age cuts for “young” (red) vs. “old” are shown; the median age (solid line), the age at which the difference between the young and old samples is maximized (minimum p -value from a two-sided Kolmogorov-Smirnov test, dashed lines), and the age which most cleanly separates the two samples (“least ambiguity”, dotted lines) are shown. Bottom: Empirical planet radii distribution for the two alternative sample cuts (to be compared with the distributions in Fig. 2), with young and old samples colored red and blue, respectively, and the line styles matching those in the top panel.

the case of the median divisor the population evolves from one with greater Neptunes to one elevated in super-Earths and depleted in sub-Neptunes, while in the case of the maximum significance, the population is initially enriched in sub-Neptunes and evolves into one with more equal numbers of sub-Neptunes and super-Earths. In the minimum ambiguity case, the older population becomes enriched in super-Earths.

We also investigated whether the observed radius evolution could be an artefact of variation in stellar properties with age that affect detection⁵. In cool stars, magnetic activity (spots and flaring) is driven by stellar rotation, and hence as stars age and spin down, the noise introduced into lightcurves by such activity decreases (e.g., Davenport 2016). This means that, all else being equal, smaller and/or more distant planets can be detected around older stars. To evaluate the magnitude of this systematic, we divided our *Kepler* late K/M dwarf sample with rotation periods in Santos et al. (2019) into 773 (older) stars more slowly rotating than the 4 Gyr M67 gyrochrone of Dungee et al. (2022), and 1936 (younger) stars more rapidly rotating than that gyrochrone; this age division is within error of our median age of 3.86 Gyr. We calculated the ratio of the detection efficiency between the moieties for each planet and plot these vs. planet radius in Fig. 4. All planets in the radius range of in-

⁵ The main sequence lifetime of stars increases with decreasing stellar mass but this is a factor only for host stars more massive than the Sun.

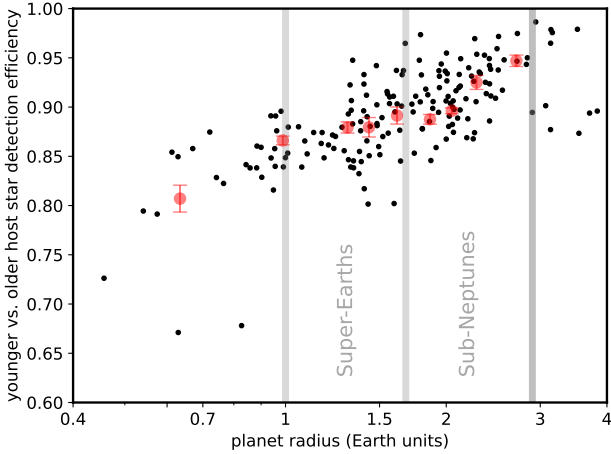


Figure 4. Ratio of mean planet detection efficiency between younger (<4 Gyr, based on rotation) and older halves of the late K and early M dwarfs observed by *Kepler*. Each point represents a planet in the KOI sample, and the red points are radius-binned averages of 20 planets with error bars representing the scatter within the bin divided by $\sqrt{20}$. The approximate radius domains of super-Earths and sub-Neptunes are delineated.

terest are slightly less detectable (by $\geq 10\%$) among the more rapidly rotating (“younger”) stars than the more slowly rotating (“older”) stars and the difference is largest among the smallest planets. However, the differential in detection efficiency between super-Earths and sub-Neptunes is $< 10\%$ and cannot explain the factor of ~ 2 difference shown in Fig. 2. (Because we are unable to adequately filter the overall sample for binary stars, which tend to be more rapidly rotating than single stars and also dilute any transit signals, we do not explicitly correct for this difference).

This observed difference in detection efficiency could possibly arise from a statistical difference in host star properties brought about selecting for stars with detectable rotation period. For example, cooler dwarf stars tend to rotate more slowly at a given age (e.g., Curtis et al. 2019) and their rotation is more difficult to detect, due both to the longer time baseline needed to capture variability and the decreasing activity leading to lower spottedness and amplitude of photometric variability. Thus, cooler, smaller stars are more likely to be included in the younger subset and this could bias transit detection statistics, although perhaps in the opposite way as observed. This effect is manifest in the difference in the T_{eff} distribution of the two subsets (Fig. 5a). However, we also find that the distribution of predicted transit signal-to-noise ratio (SNR) of the two subsets is nearly indistinguishable (Fig. 5b); the median values are 0.35 and 0.36. Here, we calculated the relative SNR for a given R_p and P_K as the inverse of the stellar radius times the square root of the brightness times the transit duration, which scales as $R_*^{-3/2} M_*^{-1/2} 10^{-m/5}$, where the *Gaia* G magnitude was used for m . Cooler dwarf stars are also intrinsically fainter, which apparently cancels out the effect of smaller radii, at least in this field.

Likewise, variation in the planet population with stellar mass combined with a difference in T_{eff} (Fig. 5a), could mimic evolution. An increasing ratio of super-Earths to sub-Neptunes with stellar mass between 0.5 and $1.4M_{\odot}$ (Fig. 12 in Petigura et al. 2022), if extending to the M dwarf range, could result in relatively fewer sub-Neptunes around stars assigned older ages. However, the variation is modest (0.04 per 0.1 dex in mass) and in our M dwarf KOI sample

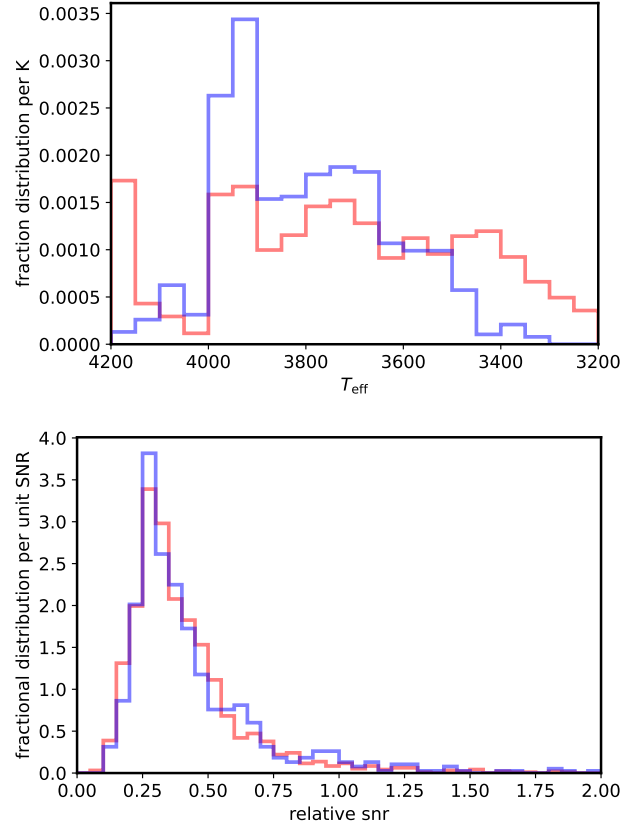


Figure 5. Top (a): Effective temperature distribution of younger (<4 Gyr, based on rotation) and older subsets of *Kepler* late K- and early M-type target stars, showing the difference due to selection effects (e.g., detectable rotation). Bottom (b): Distribution of the relative detection SNR at a given planet radius and orbital period based on a scaling with stellar parameters (see text), showing no significant difference between younger and old stars.

there is no trend between host star luminosity and age (Fig. 6) nor planet radius and host-star luminosity (Fig. 7) that would suggest such an effect. Moreover, the general trend is for less massive stars (which would preferentially populate the young subset) to have fewer super

Distributions of planet radius with orbital period and bolometric stellar irradiance or “instellation” are shown in Figs. 8 and 9, respectively. Bolometric luminosities were calculated using interpolations of the corrections to K -band luminosities tabulated in Pecaut & Mamajek (2013), and assuming near-circular orbits. We calculated the detection efficiency (i.e. fraction of planets with a given radius and period if distributed uniformly among the late K/early M type stars in our selected target sample using the procedures described in Sec. 2; this is represented as the grey contours in Fig. 8. As expected detection efficiency decreases with smaller planets on wider orbits, which explains the paucity of detections in that domain (lower right corner of Fig. 8).

4 DISCUSSION AND SUMMARY

4.1 Features of the M dwarf planet radius distribution

As has been established for planets around solar-type stars (Fulton et al. 2017) and tentatively around cooler stars (Hirano et al. 2018;

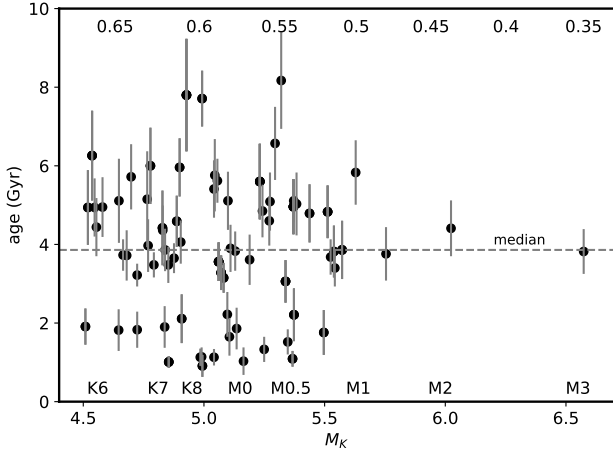


Figure 6. Distribution of gyrochronologic host star age vs. stellar luminosity (absolute K_s -band magnitude), an age-independent proxy for mass for these main sequence stars. Corresponding stellar masses and spectral types from Pecaut & Mamajek (2013) are given at the top and bottom of the plot, respectively.

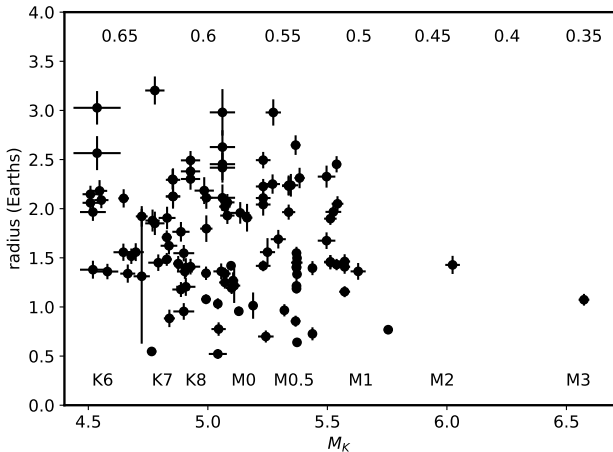


Figure 7. Planet radius vs. stellar luminosity (absolute K_s magnitude). Multi-planet systems appear as vertical chains of points.

Van Eylen et al. 2021), the radius distribution of non-Jovian *Kepler* planets orbiting late K and early M-type stars contains two peaks (super-Earths and sub-Neptunes) with an intervening gap or “valley” at $1.6\text{--}1.7R_{\oplus}$. For this sample’s median stellar mass of $0.59M_{\odot}$ and median orbital period of 7.1 days, Eqn. 11 in Ho & Van Eylen (2023) predicts a radius valley centered at $1.68 \pm 0.13 R_{\oplus}$ (vertical red lines in Fig. 2), in agreement with our derived distribution. On the other hand, the radius-period distribution (Fig. 8) suggests that the M dwarf planet radius valley is not markedly dependent on period, contrary to what has been found for solar-type stars (e.g., dashed red line in Fig. 8; Ho & Van Eylen 2023).

To quantify the slope of a linear boundary (in log-log space) for our K/M dwarf planet sample, we performed a regression of the full 180-KOI sample (including those lacking age assignments) with support vector machines (SVM) and implemented in the Python `sci-kit learn` package, with choice of regularization parameter

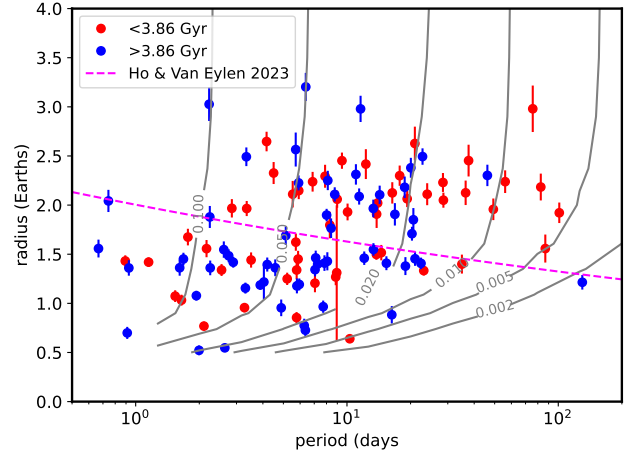


Figure 8. Radius vs. orbital period of planets in systems with ages younger (red points) or older (blue points) than the median age of the sample (3.86 Gyr). The dashed magenta line marks the center of the period-dependent radius valley for solar-type host stars determined by Ho & Van Eylen (2023). The grey contours map the *Kepler* detection efficiency (including the geometric factor) for the DR25 catalog with late K and early M dwarf host stars of all ages, i.e. the fraction of planets detected if every star in the sample hosted a planet of a given radius and orbital period.

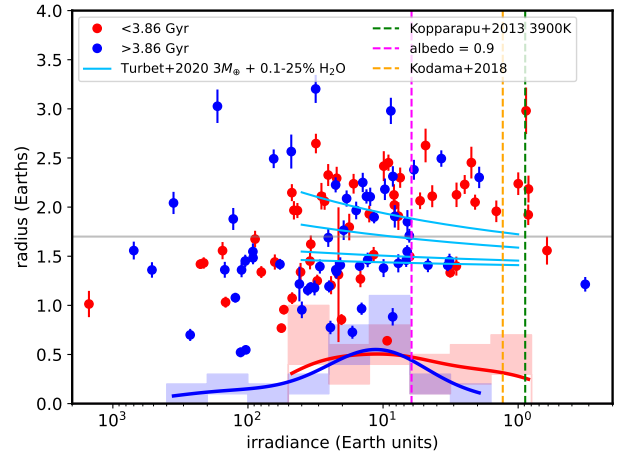


Figure 9. Radius vs. total stellar irradiance or “instellation” (in units of the current terrestrial value) for planets in systems with ages younger (red) or older (blue) than the median age of the sample (3.86 Gyr). Horizontal error bars are smaller than the points. The red/blue colored bars present histograms of young/old planets with radii of $1.7\text{--}4R_{\oplus}$, with the bars spanning the 68% probability range based on Poisson statistics. The solid red/blue curves were generated by Gaussian kernel density estimators with Scott’s bandwidth (Scott 1992). Vertical lines mark different irradiance thresholds for a runaway water vapor greenhouse atmosphere above which a planet’s atmosphere is predicted to be inflated. Cyan lines mark predicted radii of planets with a $3M_{\oplus}$ rocky core and (bottom to top) 0.1, 1, 10, and 25% H_2O mass fractions (Turbet et al. 2020).

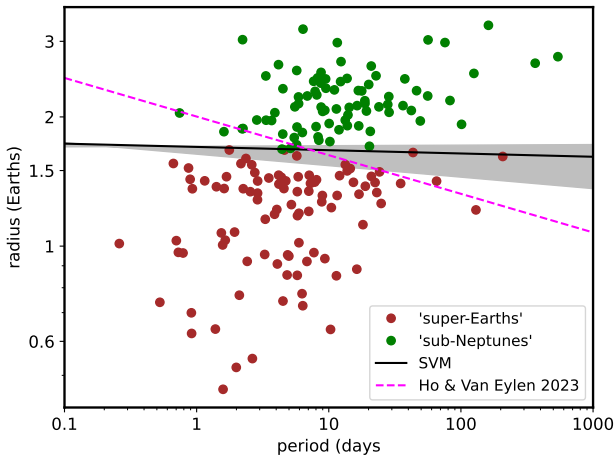


Figure 10. Linear boundary (black line) between ‘super-Earths’ and ‘sub-Neptunes’ in log period-log radius space based on a support vector machine regression, using the full K/M dwarf KOI sample (including systems without age assignments). Planets are color-coded according to the self-consistent (iterated) SVM classification and the grey region represents the 68% confidence range based on 10^4 Monte Carlo representations of the data. The Ho & Van Eylen (2023) slope is for solar-type stars.

$C = 10$, following Van Eylen et al. (2019). Classes were initially assigned simply based on radii smaller (‘sub-Neptunes’) or larger (‘super-Earths’) than $1.68R_{\oplus}$, and then iteratively re-classified (10 times) using the SVM. Confidence intervals were calculated with 10^4 Monte Carlo simulations where planet radii were randomized according to their uncertainties. We find a slope of -0.026 with a 68% confidence range of -0.043 to 0.0 , significantly flatter than the -0.09 found by Ho & Van Eylen (2023) for solar-type stars (magenta dashed line in Fig. 10). (Bonfanti et al. (2023) also report a flatter slope of -0.065 for M dwarfs.). Photo-evaporation and core-powered mass loss models predict negative slopes (see Table 6 in Ho & Van Eylen 2023), while a scenario involving planet formation under gas-depleted conditions predicts a positive slope (Lopez & Rice 2018).

Cloutier & Menou (2020) found that the planet radius distribution hosted by stars with masses $0.08\text{--}0.42M_{\odot}$ (corresponding to spectral types M3-M8) differs from that of more massive stars in lacking a significant population of (sub)Neptunes. Ment & Charbonneau (2023) also found a very pronounced dearth of sub-Neptunes around mid-to-late type M dwarfs. Our sample does not substantially overlap in stellar mass with these analyses, but there are no sub-Neptunes detected around the least luminous stars in the sample ($M_K > 5.6$) and the distribution with luminosity (Fig. 7) is at least consistent with the disappearance of sub-Neptunes at the faint end.

There is a striking paucity of planets significantly smaller than the super-Earth peak at $\approx 1.5R_{\oplus}$ (Fig. 2). Not all of this can be explained by the reduction in detection efficiency (contours in Fig. 8), suggesting that the super-Earth peak is physical. The efficient formation of relatively massive rocky planets around M dwarfs might point to a high density of solids (as ‘pebbles’, planetesimals, or protoplanets) brought about by drift/migration in the inner gas disks around M dwarfs before they are cleared (e.g., Chiang & Laughlin 2013; Chatterjee & Tan 2014; Gaidos 2017).

Distributions of planet radius with orbital period and stellar irradiance S show the absence of (sub)Neptunes on short-period or high-irradiance orbits around solar-type stars, the so-called ‘Nep-

tune desert” (Szabó & Kiss 2011; Mazeh et al. 2016). There are no universally accepted boundaries for this desert but it is expected to depend on stellar mass (McDonald et al. 2019). Adopting the conservative criteria of a period of < 2 days or $S > 300S_{\oplus}$, there is a single object in the Neptune desert around M dwarfs: KOI-952.05 (Kepler 32-f), a member of a multi-transiting planet system (Swift et al. 2013) with an orbital period of 0.74 days, has an estimated radius of $2.04 \pm 0.11R_{\oplus}$, consistent with but more precise than that determined by Morton et al. (2016) and Berger et al. (2018) but significantly larger than previous estimates (e.g., Swift et al. 2013; Mann et al. 2013). Kepler-32f would be a relevant target to measure mass and search for atmospheric escape, except that it is faint ($V = 16.4$).

Caveats and limitations of our analysis

We restricted our sample to planet host stars with detected rotational signals in *Kepler* lightcurves and these are a biased subset of the overall population. Younger stars will be rapidly rotating, magnetically active, and highly spotted and their rotational periods can be readily measured. However, due to rotational variability and intense flaring, it can be difficult to detect transiting planets (Gaidos et al. 2017). On the other hand, the oldest stars will be slowly rotating, less spotted, and exhibit less rotational variability, and the rotation periods can be similar to the *Kepler* quarterly roll (90 days) and thus more difficult to retrieve (Santos et al. 2019). This is particularly true for the coolest stars in the sample (mid M-dwarfs) because these stars have the longest rotation periods for a given age. These selection effects can manifest themselves in the overall distribution of M dwarf planet host ages (e.g., Gaidos et al. 2023b). However, we see no trend of planet properties (i.e., radius) with host star properties (i.e., luminosity, Fig. 7).

The overall occurrence rate estimated from KOIs with rotation periods could be biased upwards to the extent that stellar rotation and planetary orbits are aligned (low stellar obliquity Albrecht et al. 2022). Stars viewed at a high inclination (equator on) will have the strongest rotational signal and their planets will be more likely to transit compared to the overall population. We quantified this effect by determining the fractional numbers of KOIs around K/M dwarfs observed by *Kepler* with rotation periods in Santos et al. (2019) vs. K/M dwarfs lacking rotation periods. We applied the same cuts ($M_K > 4.5$, RUWE < 1.4 , and not otherwise identified as binaries) to both samples, but we did not apply a T_{eff} cut since temperatures are only available for the Santos et al. (2019) sample. The KOI fractions are $2.70 \pm 0.24\%$ and $2.50 \pm 0.39\%$, respectively, with uncertainties from counting statistics. These are thus indistinguishable and we conclude the effect is negligible among these types of stars, perhaps because of the high (73%) success rate of detecting rotation among these stars.

Transit parameters and stellar parameters were not computed self-consistently (the former assuming DR25 values and the latter based on revised luminosities and new empirical relations). Stellar density is covariant with transit impact parameter which, along with T_{eff} (which controls limb darkening coefficients) is covariant with the planet-to-star radius ratio R_p/R_* . Lastly, our filtering of binaries from the *Kepler* late K- and early M-dwarf target sample was less thorough since AO imaging is not available for the overall *Kepler* K/M dwarf population as it is for the KOIs.

4.2 Clues to the nature of sub-Neptunes

The decline of the sub-Neptune population relative to super-Earths between the younger (< 3.8 Gyr) and older halves of our sample of late K and early M dwarf-hosted planets (Fig. 2), is analogous to

what has been found among solar-type *Kepler* host stars (Berger et al. 2020; Sandoval et al. 2021; David et al. 2021; Chen et al. 2022). Berger et al. (2020) found a decline in the sub-Neptune peak in stars older than fiducial age of the Hyades (≈ 650 Myr) relative to younger stars, and interpreted this evolution in terms of the escape of H/He-rich envelopes. The Gyr timescale implied was seen as more supportive of the core-powered mechanism for mass-loss (Gupta & Schlichting 2021) over photo-evaporative escape (Owen 2019). The decline in sub-Neptunes between the younger and older halves of our sample of late-type host stars suggest a multi-Gyr timescale, and perhaps the same mechanism in operation around these lower-mass stars.

Figure 8 compares the period-radius distribution of the younger (red points) and older (blue points) halves of the sample. While there are both younger and older sub-Neptunes ($> 1.68R_{\oplus}$, above the horizontal line) at periods < 24 days, nearly all those at longer periods (> 24 days) are in the younger half of the sample. The phenomenon manifests itself in a plot of stellar irradiance vs. radius (Fig. 9). The fraction of older sub-Neptunes in the sample falls from 54% at irradiances $> 5S_{\oplus}$ to 15% at lower irradiance (see red and blue histograms). There are no sub-Neptunes in the sample below an irradiance of $1 S_{\oplus}$, although this could be due in part to low detection efficiency at long orbital periods. The two planets that are marginally less irradiated are KOIs 812.03 (Kepler 235-e) and 952.03 (Kepler 32-d), with ages of 7.8 ± 1.43 and 5.60 ± 0.96 Gyr, respectively (Gaidos et al. 2023b).

The disappearance of sub-Neptunes over several Gyr could be explained by thermal contraction of atmospheres combined with escape of H and He to space (Howe & Burrows 2015, e.g.,). This evolution ultimately leaves super-Earth-sized cores, which on wider ($P > 20$ day) orbits are unlikely to be detected (grey contours in Fig. 8). However, this would not explain the relative abundance of older sub-Neptunes on closer orbits, where irradiation is higher and the process of evaporation and escape should be more rapid. One possibility is that the apparent dependence of sub-Neptune evolution on orbital period and irradiance is a selection effect, i.e. a combination of correlations of age with host star mass/luminosity, and host star mass and planet period distribution. There is, however no evidence for either correlation (Figs. 6 and 11).

The persistence of “warm” sub-Neptunes at older ages could be due to an inflation mechanism that is depends on the planet’s irradiation or equilibrium temperature and hence proximity to the host star. Turbet et al. (2020) showed that (primarily) rocky planets with water-dominated runaway greenhouse atmospheres could have sub-Neptune-like radii. Both Kopparapu et al. (2013) and Turbet et al. (2019) found the irradiance threshold for a runaway greenhouse on an Earth-like planet to be about 1.05 the present terrestrial value S_{\oplus} , while atmospheres containing significant H/He will have a lower threshold (Innes et al. 2023). Around M dwarfs stars the threshold is slightly lower because of reduced Rayleigh scattering and increased absorption by atmospheric H_2O at the longer wavelengths where cooler stars emit more radiation; the value is predicted to be $0.9 S_{\oplus}$ for $T_{\text{eff}}=3900\text{K}$ (M0 spectral type) (red line in Fig. 9). Three-dimensional general circulation models put the threshold somewhat higher and dependent on rotation rate (Leconte et al. 2013; Kodama et al. 2018, ; vertical orange dashed line in Fig. 9).

A significantly elevated runaway threshold could be produced by a much higher elevated Bond albedo of a cloudy steam atmosphere; that of Venus is around 0.76 (Moroz et al. 1985) but measurements of the phase function suggest a value as high as 0.9 (Mallama et al. 2006). This would move the runaway threshold

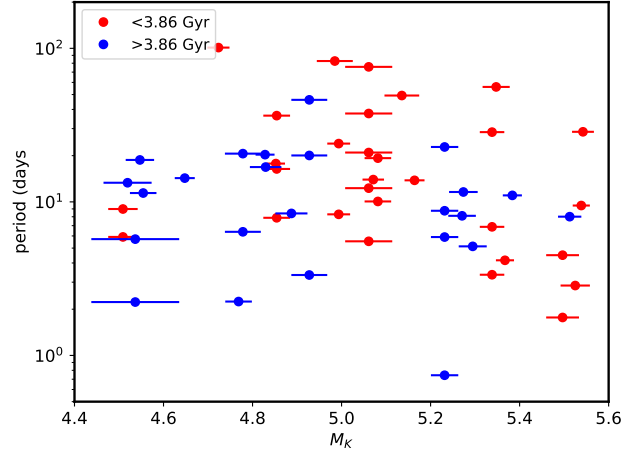


Figure 11. Orbital period vs. host star luminosity (M_K) for younger (red) and older (blue) sub-Neptunes (planets with radii between 1.7 and $4R_{\oplus}$). There is no correlation that could explain the absence of older sub-Neptunes at larger radii.

to $\sim 5S_{\oplus}$, the approximate boundary where sub-Neptunes become persistent (vertical dashed magenta line in Fig. 9).⁶

Figure 9 includes predicted radius vs. irradiance for planets with $3M_{\oplus}$ rocky cores and H_2O mass fractions between 0.1 and 25% (Turbet et al. 2020), with the core mass chosen to reproduce the observed $1.5 R_{\oplus}$ population. Water mass fractions $\gg 25\%$ would be needed to explain some objects. Water-rich planets have been invoked to explain the sub-Neptune population with radii up to $3R_{\oplus}$ (Burn et al. 2024), but Vivien et al. (2022) found that pure water/steam atmospheres on sub-Earths become unstable if the atmospheric scale height exceeds 0.1 times the planet radius. The radii of some sub-Neptunes might also require significant H/He to explain, especially those of planets at larger separations; H/He lowers the mean molecular weight and decreases the irradiance threshold for a runaway water-vapor greenhouse (Innes et al. 2023). The rate of H/He escape would then control the (Gyr) timescale over which sub-Neptunes on orbits beyond the pure-water vapor runaway threshold shrink and became undetectable by *Kepler*. Escape of H/He from hotter sub-Neptunes inside the threshold might be slowed by dilution and cooling by H_2O vapor (Yoshida et al. 2022), or counterbalanced by permanent magma oceans that act as a sink for oxygen released by UV photolysis of H_2O and thus a source for H (Schaefer et al. 2016).

We investigated whether irradiance-dependent evolution of sub-Neptunes also appears in the sample of *Kepler* transiting planets around solar-type host stars with isochrone ages determined by Berger et al. (2018). We restrict the sample to those with ages more precise than 30%, and although the median age of the sample is 5 Gyr, we use the same division of 3.86 Gyr between young and old populations for comparison. No such effect is obvious in the distribution of planets with irradiance (Fig. 12). The ratio of young to old planets is statistically indistinguishable (≈ 0.44) for planets experiencing $S > 5S_{\oplus}$ and $S < 5S_{\oplus}$. Three explanations for the difference between the late K/early M dwarf sample and solar-type

⁶ The albedo depends would depend strongly on cloud droplet size and the high reflectivity of Venus is largely due to sulfuric acid aerosols and a similar scenario might not apply to steam atmospheres.

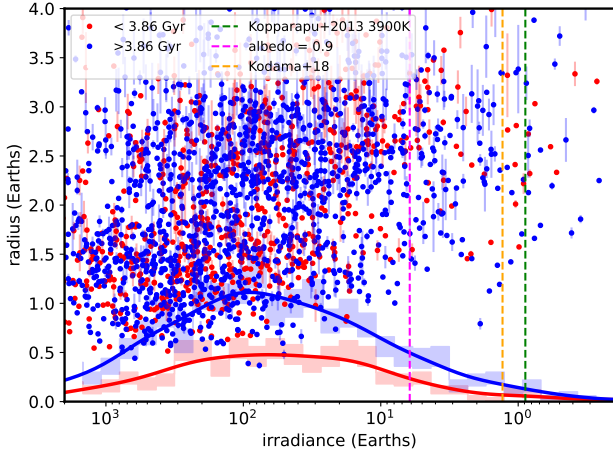


Figure 12. Distributions of planet radius vs. stellar irradiation for systems around solar-type stars with ages that are younger (red points) or older (blue points) than 3.86 Gyr, from Berger et al. (2018). Compare to Fig. 9 for late K and early M-type stars. Here, systematic errors in irradiance are likely larger than counting statistics.

stars are (1) the former is affected by small-number statistics and is a spurious result; (2) the ages of the Berger et al. (2018) sub-sample with relatively cool planets are more uncertain because the host stars are likely to be late G and early K dwarfs which evolve very slowly; and (3) there is a fundamental difference in the two populations of planets around these stars. Planets at a given bolometric irradiance S around M dwarfs will experience far more X-ray and UV irradiation than their solar-type counterparts (McDonald et al. 2019) and it is this radiation that drives photoevaporation of H/He atmospheres (Owen 2019). Thus temperate sub-Neptunes around solar-type stars may be dominated by cores with H/He atmospheres, while those around M dwarfs have lost most or all H/He and their radii are controlled by the behavior of water-dominated atmospheres. Measurements of planet mass by RVs and observations of atmospheres by *JWST* for examples around much closer, brighter host stars could distinguish between these scenarios.

There are six planets in the sample with irradiances less than S_{\oplus} and could be considered to orbit within the “habitable zones” of their host stars, but only two of these are super-Earth-sized: KOIs 571.05 (Kepler-186f Quintana et al. 2014), with a radius of $1.21 \pm 0.07 R_{\oplus}$ and a gyrochronologic system age of 5.0 ± 0.7 Gyr, and KOI-2418.01 (Kepler-1229b, Morton et al. 2016), with a radius of $1.56 \pm 0.14 R_{\oplus}$ and a gyrochronologic system age of 1.3 ± 0.3 Gyr.

Our findings, while intriguing, are limited in their statistical robustness not by the precision with which stellar and planet parameters can be determined, but by sample size, the small number of late K and M dwarf systems being a product of the selection criteria for targets of the *Kepler* prime mission and the telescope’s single fixed pointing. Both the *K2* and *TESS* mission have identified many more transiting planet systems around such stars, some of which have ages assigned by gyrochronology (Gaidos et al. 2023b). However, determining the rotation periods of late-type field stars from *K2* or *TESS* photometry alone remains challenging (Reinhold & Hekker 2020; Claytor et al. 2022). The *PLATO* mission and its long-duration (≥ 1 year) observation phase fields should yield additional systems with gyrochronologic ages, but only among K dwarfs (Nascimbeni et al. 2022). There are also additional investigations that could be performed with larger samples, for example, the ex-

Table 1. *Kepler* M Dwarf Planet Radii and Ages¹

Name	Radius R_{\oplus}	Age Gyr
KOI-247.01	1.91 +0.10/-0.11	1.03±0.35
KOI-251.01	2.65 +0.10/-0.10	1.09±0.20
KOI-251.02	0.85 +0.05/-0.05	1.09±0.20
KOI-253.01	3.20 +0.13/-0.13	6.00±0.97
KOI-253.02	1.85 +0.10/-0.11	6.00±0.97
KOI-254.01	11.54 +0.35/-0.35	1.14±0.24
KOI-314.01	1.50 +0.05/-0.05	2.21±0.67
KOI-314.02	1.33 +0.05/-0.05	2.21±0.67
KOI-314.03	0.64 +0.03/-0.03	2.21±0.67
KOI-430.01	2.69 +0.10/-0.10	—

¹The full table is available as a machine-readable table (<http://zenodo.org>).

pected dynamical evolution of multi-planet systems due to mutual perturbations (Teixeira & Ballard 2023).⁷

ACKNOWLEDGEMENTS

EG and AA acknowledge support from the NASA Exoplanet Research Program (Award 80NSSC20K0957). ALK acknowledges support from the NASA Exoplanet Research Program (Award 80NSSC22K0781). Some of the data presented herein were obtained at the W. M. Keck Observatory, which is operated as a scientific partnership among the California Institute of Technology, the University of California and the National Aeronautics and Space Administration. The Observatory was made possible by the generous financial support of the W. M. Keck Foundation. This research has made use of the NASA Exoplanet Archive, which is operated by the California Institute of Technology, under contract with the National Aeronautics and Space Administration under the Exoplanet Exploration Program. This work has made use of data from the European Space Agency (ESA) mission *Gaia* (<https://www.cosmos.esa.int/gaia>), processed by the *Gaia* Data Processing and Analysis Consortium (DPAC, <https://www.cosmos.esa.int/web/gaia/dpac/consortium>). Funding for the DPAC has been provided by national institutions, in particular, the institutions participating in the *Gaia* Multilateral Agreement.

DATA AVAILABILITY

The KIC and DR25 KOI catalogs are available from the, *Gaia* DR3 astrometry and photometry are available from the CDS, and AO imaging is publicly available from the Keck Observatory Archive.

REFERENCES

Albrecht S. H., Dawson R. I., Winn J. N., 2022, *PASP*, 134, 082001

⁷ The orbital period distributions of the young and old sub-samples presented here do not appear significantly different (K-S test $p = 0.15$).

- Barnes R., Jackson B., Raymond S. N., West A. A., Greenberg R., 2009, *ApJ*, 695, 1006
- Batalha N. M., et al., 2013, *ApJS*, 204, 24
- Belokurov V., et al., 2020, *MNRAS*, 496, 1922
- Berger T. A., Howard A. W., Boesgaard A. M., 2018, *ApJ*, 855, 115
- Berger T. A., Huber D., van Saders J. L., Gaidos E., Tayar J., Kraus A. L., 2020, *AJ*, 159, 280
- Béthune W., Rafikov R. R., 2019, *MNRAS*, 488, 2365
- Bonfanti A., et al., 2023, arXiv e-prints, p. arXiv:2311.12577
- Borucki W. J., et al., 2010, *Science*, 327, 977
- Brown T. M., Latham D. W., Everett M. E., Esquerdo G. A., 2011, *AJ*, 142, 112
- Bryson S., et al., 2021, *AJ*, 161, 36
- Burke C. J., Catanzarite J., 2017a, Planet Detection Metrics: Window and One-Sigma Depth Functions for Data Release 25, Kepler Science Document KSCI-19101-002, id. 14. Edited by Michael R. Haas and Natalie M. Batalha
- Burke C. J., Catanzarite J., 2017b, Planet Detection Metrics: Per-Target Detection Contours for Data Release 25, Kepler Science Document KSCI-19111-002, id. 19. Edited by Michael R. Haas and Natalie M. Batalha
- Burke C. J., et al., 2015, *ApJ*, 809, 8
- Burn R., Mordasini C., Mishra L., Haldemann J., Venturini J., Emsenhuber A., Henning T., 2024, *Nature Astronomy*,
- Chatterjee S., Tan J. C., 2014, *ApJ*, 780, 53
- Chen D.-C., et al., 2022, *AJ*, 163, 249
- Chiang E., Laughlin G., 2013, *MNRAS*, 431, 3444
- Christiansen J. L., et al., 2012, *PASP*, 124, 1279
- Claytor Z. R., van Saders J. L., Llama J., Sadowski P., Quach B., Avallone E. A., 2022, *ApJ*, 927, 219
- Cloutier R., Menou K., 2020, *AJ*, 159, 211
- Curtis J. L., Agüeros M. A., Douglas S. T., Meibom S., 2019, *ApJ*, 879, 49
- Cutri R. M., et al., 2013, Technical report, Explanatory Supplement to the AllWISE Data Release Products. IPAC/Caltech
- Davenport J. R. A., 2016, *ApJ*, 829, 23
- David T. J., et al., 2021, *AJ*, 161, 265
- Dressing C. D., Charbonneau D., 2015, *ApJ*, 807, 45
- Dungee R., van Saders J., Gaidos E., Chun M., García R. A., Magnier E. A., Mathur S., Santos Á. R. G., 2022, *ApJ*, 938, 118
- El-Badry K., Rix H.-W., 2018, *MNRAS*, 480, 4884
- El-Badry K., Rix H.-W., Heintz T. M., 2021, *MNRAS*, 506, 2269
- Fulton B. J., et al., 2017, *AJ*, 154, 109
- Gaia Collaboration et al., 2016, *A&A*, 595, A1
- Gaia Collaboration et al., 2023, *A&A*, 674, A1
- Gaidos E., 2017, *MNRAS*, 470, L1
- Gaidos E., Mann A. W., Kraus A. L., Ireland M., 2016, *MNRAS*, 457, 2877
- Gaidos E., et al., 2017, *MNRAS*, 464, 850
- Gaidos E., et al., 2023a, *MNRAS*, 518, 3777
- Gaidos E., Claytor Z., Dungee R., Ali A., Feiden G. A., 2023b, *MNRAS*, 520, 5283
- Greene T. P., Bell T. J., Ducrot E., Dyrek A., Lagage P.-O., Fortney J. J., 2023, *Nature*, 618, 39
- Gupta A., Schlichting H. E., 2021, *MNRAS*, 504, 4634
- Hardegree-Ullman K. K., Cushing M. C., Muirhead P. S., Christiansen J. L., 2019, *AJ*, 158, 75
- Hirano T., et al., 2018, *AJ*, 155, 127
- Ho C. S. K., Van Eylen V., 2023, *MNRAS*, 519, 4056
- Hoffman Kelsey L., Rowe J. F., 2017, Uniform Modeling of KOIs: MCMC Notes for Data Release 25, Kepler Science Document KSCI-19113-001, id. 21. Edited by Michael R. Haas and Natalie M. Batalha
- Howard A. W., et al., 2012, *ApJS*, 201, 15
- Howe A. R., Burrows A., 2015, *ApJ*, 808, 150
- Hsu D. C., Ford E. B., Ragozzine D., Ashby K., 2019, *AJ*, 158, 109
- Innes H., Tsai S.-M., Pierrehumbert R. T., 2023, arXiv e-prints, p. arXiv:2304.02698
- Johnson J. A., et al., 2012, *AJ*, 143, 111
- Johnstone C. P., Bartel M., Güdel M., 2021, *A&A*, 649, A96
- Kanodia S., Wolfgang A., Stefansson G. K., Ning B., Mahadevan S., 2019, *ApJ*, 882, 38
- Kodama T., Nitta A., Genda H., Takao Y., O'ishi R., Abe-Ouchi A., Abe Y., 2018, *Journal of Geophysical Research (Planets)*, 123, 559
- Kopparapu R. K., et al., 2013, *ApJ*, 765, 131
- Kraus A. L., Ireland M. J., Huber D., Mann A. W., Dupuy T. J., 2016, *AJ*, 152, 8
- Leconte J., Forget F., Charnay B., Wordsworth R., Pottier A., 2013, *Nature*, 504, 268
- Lindgren L., et al., 2018, *A&A*, 616, A2
- Lopez E. D., Rice K., 2018, *MNRAS*, 479, 5303
- Luque R., Pallé E., 2022, *Science*, 377, 1211
- Mallama A., Wang D., Howard R. A., 2006, *Icarus*, 182, 10
- Mann A. W., Gaidos E., Ansdell M., 2013, *ApJ*, 779, 188
- Mann A. W., Feiden G. A., Gaidos E., Boyajian T., von Braun K., 2015, *ApJ*, 804, 64
- Mann A. W., et al., 2019, *ApJ*, 871, 63
- Mathur S., et al., 2017, *ApJS*, 229, 30
- Mazeh T., Holczer T., Faigler S., 2016, *A&A*, 589, A75
- McDonald G. D., Kreidberg L., Lopez E., 2019, *ApJ*, 876, 22
- McLean I. S., Chaffee F. H., 2000, in Iye M., Moorwood A. F., eds, Society of Photo-Optical Instrumentation Engineers (SPIE) Conference Series Vol. 4008, Optical and IR Telescope Instrumentation and Detectors. pp 2–7, doi:10.1117/12.395404
- Ment K., Charbonneau D., 2023, *AJ*, 165, 265
- Messina S., et al., 2017, *A&A*, 607, A3
- Moroz V. I., et al., 1985, *Advances in Space Research*, 5, 197
- Morton T. D., Bryson S. T., Coughlin J. L., Rowe J. F., Ravichandran G., Petigura E. A., Haas M. R., Batalha N. M., 2016, *ApJ*, 822, 86
- Mulders G. D., Pascucci I., Apai D., 2015, *ApJ*, 798, 112
- Nascimbeni V., et al., 2022, *A&A*, 658, A31
- Owen J. E., 2019, *Annual Review of Earth and Planetary Sciences*, 47, 67
- Owen J. E., Wu Y., 2013, *ApJ*, 775, 105
- Pecaut M. J., Mamajek E. E., 2013, *ApJS*, 208, 9
- Petigura E. A., et al., 2022, *AJ*, 163, 179
- Quintana E. V., et al., 2014, *Science*, 344, 277
- Ravinot T., Lagarde N., Reylé C., Amard L., Van Grootel V., 2022, in Cambridge Workshop on Cool Stars, Stellar Systems, and the Sun. Cambridge Workshop on Cool Stars, Stellar Systems, and the Sun. p. 166, doi:10.5281/zenodo.7586227
- Reinhold T., Hekker S., 2020, *A&A*, 635, A43
- Rogers L. A., 2015, *ApJ*, 801, 41
- Rogers L. A., Seager S., 2010, *ApJ*, 712, 974
- Sandoval A., Contardo G., David T. J., 2021, *ApJ*, 911, 117
- Santos A. R. G., García R. A., Mathur S., Bugnet L., van Saders J. L., Metcalfe T. S., Simonian G. V. A., Pinsonneault M. H., 2019, *ApJS*, 244, 21
- Schaefer L., Wordsworth R. D., Berta-Thompson Z., Sasselov D., 2016, *ApJ*, 829, 63
- Scott D. W., 1992, *Multivariate Density Estimation*. John Wiley & Sons
- Silverberg S. M., et al., 2020, *ApJ*, 890, 106
- Skrutskie M. F., et al., 2006, *AJ*, 131, 1163
- Skumanich A., 1972, *ApJ*, 171, 565
- Smart R., et al., 2021, in The 20.5th Cambridge Workshop on Cool Stars, Stellar Systems, and the Sun (CS20.5). Cambridge Workshop on Cool Stars, Stellar Systems, and the Sun. p. 81, doi:10.5281/zenodo.4562738
- Stauffer J., Rebull L. M., Cody A. M., Hillenbrand L. A., Pinsonneault M., Barrado D., Bouvier J., David T., 2018, *AJ*, 156, 275
- Sullivan K., et al., 2023, *AJ*, 165, 177
- Swift J., Johnson J. A., Morton T., Crepp J. R., Montet B., Fabrycky D. C., Muirhead P., 2013, in American Astronomical Society Meeting Abstracts #221. p. 407.04
- Szabó G. M., Kiss L. L., 2011, *ApJ*, 727, L44
- Tabone B., et al., 2023, *Nature Astronomy*, 7, 805
- Teixeira K., Ballard S., 2023, *ApJ*, 953, 50
- Thompson S. E., et al., 2018, *ApJS*, 235, 38
- Tonry J. L., et al., 2012, *ApJ*, 750, 99

- Turbet M., Ehrenreich D., Lovis C., Bolmont E., Fauchez T., 2019, *A&A*, 628, A12
- Turbet M., Bolmont E., Ehrenreich D., Gratier P., Leconte J., Selsis F., Hara N., Lovis C., 2020, *A&A*, 638, A41
- Valizadegan H., Martinho M. J. S., Jenkins J. M., Caldwell D. A., Twicken J. D., Bryson S. T., 2023, *AJ*, 166, 28
- Van Eylen V., et al., 2019, *AJ*, 157, 61
- Van Eylen V., et al., 2021, *MNRAS*, 507, 2154
- Vivien H. G., Aguichine A., Mousis O., Deleuil M., Marcq E., 2022, *ApJ*, 931, 143
- Weiss L. M., Marcy G. W., 2014, *ApJ*, 783, L6
- Weiss L. M., et al., 2018, *AJ*, 155, 48
- Yoshida T., Terada N., Ikoma M., Kuramoto K., 2022, *ApJ*, 934, 137
- Zhu W., Dong S., 2021, *ARA&A*, 59, 291
- Zieba S., et al., 2023, arXiv e-prints, p. arXiv:2306.10150
- Ziegler C., et al., 2018a, *AJ*, 156, 83
- Ziegler C., et al., 2018b, *AJ*, 156, 259

This paper has been typeset from a $\text{\TeX}/\text{\LaTeX}$ file prepared by the author.